



Electrochemical energy storage behavior of Sn/SnO₂ double phase nanocomposite anodes produced on the multiwalled carbon nanotube buckypapers for lithium-ion batteries



Mirac Alaf*, Hatem Akbulut

Sakarya University, Engineering Faculty, Dept. of Metallurgy and Materials Engineering, Esentepe Campus, 54187 Sakarya, Turkey

HIGHLIGHTS

- Free-standing Sn/SnO₂/MWCNT electrodes were produced for Li-ion batteries.
- Controllable Sn/SnO₂ core–shell double phase structures were achieved.
- Gradient nanocomposite electrodes produced on the MWCNT buckypapers.
- Sn/SnO₂/MWCNT electrodes prevented a capacity of 624 mAh g⁻¹ even after 100 cycles.

ARTICLE INFO

Article history:

Received 31 May 2013

Received in revised form

22 August 2013

Accepted 4 September 2013

Available online 19 September 2013

Keywords:

Lithium-ion batteries

Tin oxide

Nanocomposite

Core–shell structure

Energy storage

ABSTRACT

Recent development of electrode materials for Li-ion batteries is driven mainly by hybrid nanocomposite structures consisting of Li storage compounds and CNTs. In this study, tin/tin oxide (Sn/SnO₂) films and tin/tin oxide/multi walled carbon nanotube (Sn/SnO₂/MWCNT) nanocomposites are produced by a two steps process; thermal evaporation and subsequent plasma oxidation as anode materials for Li-ion batteries. The physical, structural, and electrochemical behaviors of the nanocomposite electrodes containing MWCNTs are discussed. The ratio between metallic tin (Sn) and tin oxide (SnO₂) is controlled with plasma oxidation time and effects of the ratio are investigated on the structural and electrochemical properties. The greatly enhanced electrochemical performance is mainly due to the morphological stability and reduced diffusion resistance, which are induced by MWCNT core and deposited Sn/SnO₂ double phase shell. The outstanding long-term cycling stability is a result of the two layers Sn and SnO₂ phases on MWCNTs. The nanoscale Sn/SnO₂/MWCNT network provides good electrical conductivity, and the creation of open spaces that buffer a large volume change during the Li-alloying/de-alloying reaction.

© 2013 Elsevier B.V. All rights reserved.

1. Introduction

Lithium-ion batteries (LIBs) offer significant advantages in weight and energy density over other rechargeable batteries. They have proven to be ideal for small-scale portable electronic applications such as cellular phones and laptop computers. Emerging applications in implantable medical devices also take advantage of the high cycle life, light weight and other benefits of LIBs [1,2]. However, alternative forms of transportation, such as plug-in hybrid electric vehicles (PHEV) and all electric vehicles (EV),

require significant improvements in many perspectives, such as energy density, safety, durability and cost [3].

Tin, as a candidate anode material of lithium-ion batteries, has received much attention because of its much higher specific capacity (994 mAh g⁻¹) than that of commercially used graphite (372 mAh g⁻¹). Later, crystallographic studies suggested that the realistic form of this end phase could be Li₁₇Sn₄ (thus, 4.25 Li per Sn) [4,5]. The potential of the tin-based anodes is slightly higher than that of graphite, which reduces the potential safety problems with metallic lithium deposition on the host anode, which occurs during rapid charging and discharging [3]. Similarly, among LIBs anode materials, SnO₂-based materials have become one of the other promising candidates, as SnO₂ has high theoretical capacity, the environmental friendliness of its raw material processing and low cost. In theory, SnO₂ exhibits a first discharge capacity of

* Corresponding author. Tel.: +90 264 295 6722; fax: +90 264 295 56 01.

E-mail address: mirackumas@yahoo.com (M. Alaf).

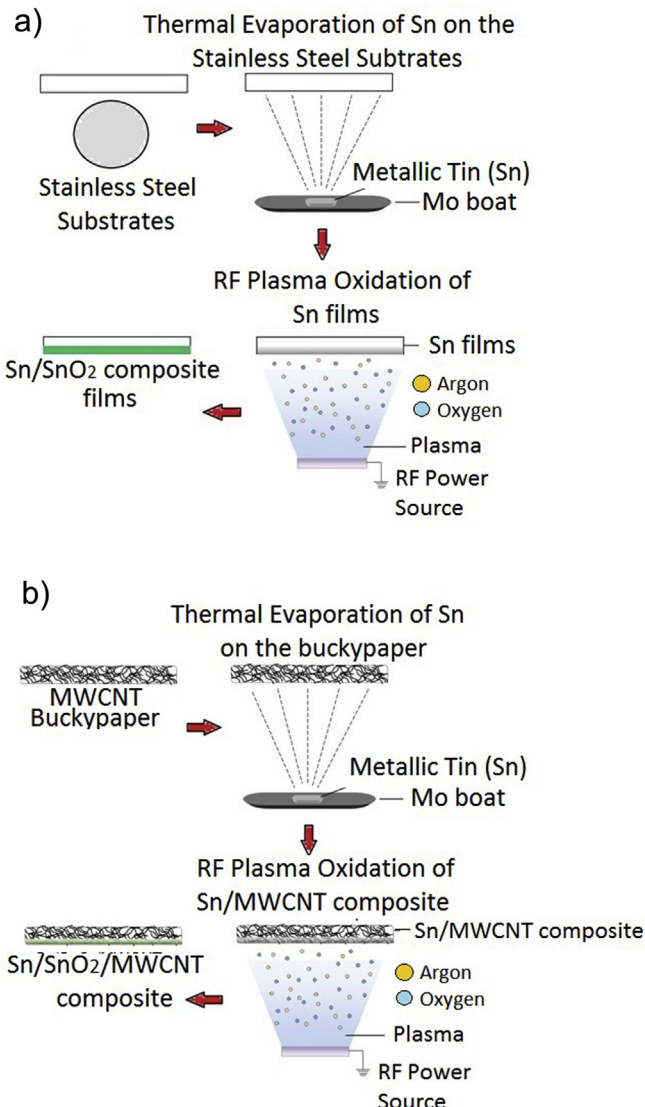


Fig. 1. Schematic representations of the route for preparing (a) Sn/SnO₂ and (b) Sn/SnO₂/MWCNT nanocomposites.

1494 mAh g⁻¹ and a reversible discharge capacity of 782 mAh g⁻¹ [6]. It has been proven that the bulk tin based materials could easily crack during cycling, which would directly increase the resistance of the electrode. Many efforts have been made to improve the capacitance and the cycle ability of the tin-based material. Up to now, there are mainly two strategies: one is to make tin-based alloys and other is to produce nanocomposite electrodes [7].

These two strategies are applied since tin based anodes are plagued by the large volume change of these metals during lithium insertion/extraction. Decrepitizing or fracture of particles in an electrode into smaller pieces normally happens during the intercalation/de-intercalation of lithium ions. About a 360% volume expansion of pure tin causes the internal strain of the materials [3,8]. The large volume variation leads to the pulverization of the electrode and the loss of electrical contact between the active Sn and conductive additives or the current collector performance [9–11]. In addition, previous studies have revealed that the SnO₂ anode may electrochemically react with lithium ions, leading to the formation of small and active Sn particles that are easy to aggregate into larger and inactive tin clusters during

lithium alloying and de-alloying [12]. All these factors result in deterioration of the electrode structure and decay of electrochemical property.

To alleviate the negative effect of the volume change, different approaches have been put forward to modify the morphology and structure of SnO₂, including fabricating nano-sized SnO₂ [13], introducing mesopores [14] and incorporating SnO₂ into other active or inactive materials to form composites [15]. A more effective way is to combine these approaches. Nanostructured SnO₂ provides high capacity and largely reduced diffusion length for lithium ions, while the carbon nanotubes enhance electrical contact, facilitating charge transfer and also acts as a buffer to accommodate the volume change of SnO₂ [16].

Using of Sn/SnO₂ composites could be a solution in realizing increased reversible capacity as well as reduced irreversible capacity and capacity fade upon cycling, as this could increase the Sn:Li₂O ratio in the anode matrix [17]. Other effective strategies to alleviate this problem is to disperse tin based materials in a carbon matrix or encapsulate them with carbon to accommodate the strain of volume change during the alloying and de-alloying processes of Li–Sn. Among them, the tin based matrix/carbon nanotube (CNT) composites have attracted considerable research effort [18]. CNTs, because of their unique 1D tubular structure, high electrical and thermal conductivities, high elastic behavior and extremely large surface area, have been considered as ideal additive materials to improve the electrochemical characteristics of the electrode of LIBs. CNT based electrode materials have been recently studied by many research groups [19]. Using the elastic binder can significantly improve the capacity retention of the electrodes with amorphous alloy anode materials [20]. Similarly, the SnO₂-based electrodes also suffer from the large mechanical stress induced by volume change during the subsequent alloying/de-alloying process. Therefore, the elastic binder is expected to show a positive effect on the electrochemical performance of the SnO₂-based anodes. The matrix acts as not only a dispersant to prevent the aggregation of active SnO₂ nanoparticles, but also an inactive confining buffer to accommodate the volume change during the cycling [21]. Among various nanocomposites, SnO₂–carbon composites, especially those with a core–shell structure, are considered to be promising to restrain the pulverization of SnO₂ and prevent tin particle aggregation and disconnection from the conductive additives or the current collector, because the carbon layer exhibits flexibility, good electronic conductivity and excellent compatibility with the electrode, which can improve the conductivity and buffer the mechanical stress induced by the huge volume variation of SnO₂ during the repeated lithium intercalation–deintercalation processes [22–25].

Sn based oxide electrodes have shown better cycling performance than metallic Sn electrode, although the capacity fade upon repeated cycles is still observed in Sn oxide electrodes. It was claimed that Sn atoms aggregated in certain voltage range during cycling, and the coexistence between the Sn aggregates and Li–Sn alloy phases caused fracturing, and eventual capacity fade upon cycling [26]. Since the overall Sn aggregation process was well documented in many previous studies, the present study focuses on the new findings, which were not addressed in the past works. In our present work, double phase Sn/SnO₂ nanocomposite films and Sn/SnO₂/MWCNT core–shell nanocomposites were produced by thermal evaporation and subsequent plasma oxidation as anode materials for LIBs. The effect of Sn/SnO₂ ratio on the stainless steel substrate and MWCNT buckypapers is aimed to investigate. The ratio between metallic tin (Sn) and tin oxide (SnO₂) was controlled with plasma oxidation time and effects of the ratio were investigated on the morphological and electrochemical properties.

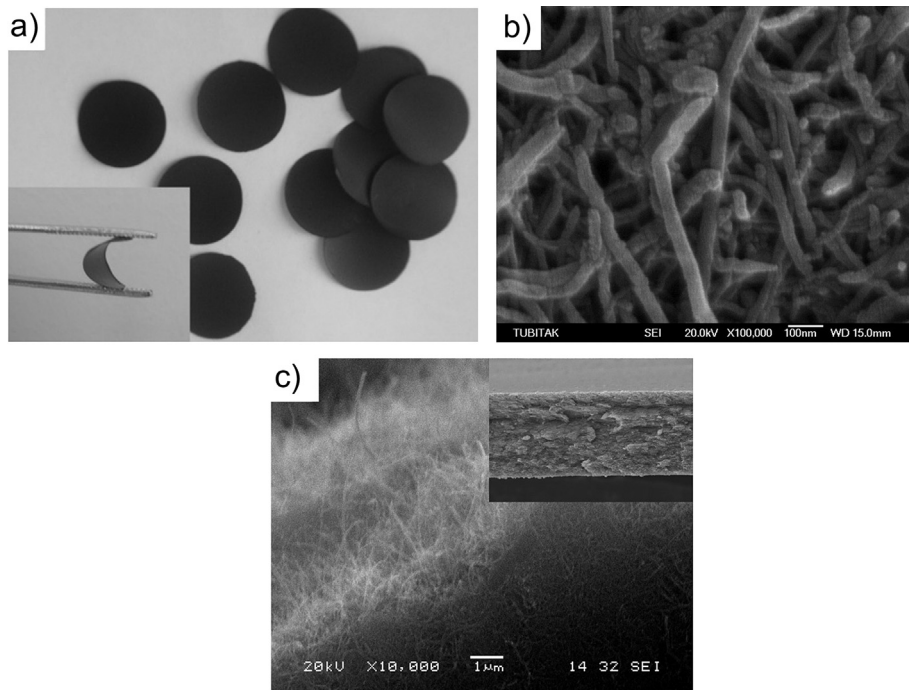


Fig. 2. a) Flexible free-standing MWCNT buckypapers, b) FESEM image of buckypaper and c) cross-section.

2. Experiment details

2.1. Chemical oxidation of MWCNT and preparing of buckypapers

MWCNTs over 1.0 μm in length with the outer diameter of 50 nm were purchased from Arry Nano (Germany). Since the mechanical properties of buckypapers are primarily determined by the tube–tube interactions, chemical oxidation of the MWCNT sidewalls and tips could be utilized to increase the modulus and strength of the MWCNT buckypapers. Chemical oxidation of MWCNTs was carried out with a mixture of H₂SO₄ and HNO₃ acids in the ratio of 3:1 for 3 h after annealing and treating in HCl acid for impurity removing. The oxidized MWCNTs were first dispersed into water by the aid of SDS surfactant and sonicated to form a well-dispersed suspension, which was subsequently vacuum filtered through PVDF membrane filters with 220 nm pore size to form buckypapers. In each experiment, a MWCNT suspension at a concentration of 1 mg ml⁻¹ was prepared by tip sonication for 60 min. Then the resulting solid was washed up, and the sample dried in the vacuum at 40 °C for overnight, and the MWCNT films were peeled-off from the filtration membrane.

2.2. Production Sn/SnO₂ and Sn/SnO₂/MWCNT nanocomposites via thermal evaporation and RF plasma oxidation

Thermal evaporation of metallic tin on the stainless steel substrates and buckypapers was performed in a multifunctional PVD unit. High purity metallic tin (99.999%) was placed in a tungsten (W) boat in the deposition chamber, which was evacuated to 10⁻⁴ Pa and then backfilled with argon to a pressure of 1 Pa to produce Sn films and Sn/MWCNT nanocomposites. Evaporation was carried out at 100 A current. Evaporation time was chosen as 1 min for producing a shell layer of metallic tin on the functionalized surfaces of MWCNTs. Sn thin films in the thickness of 500 nm were deposited onto stainless steel substrates. Sn/SnO₂ and Sn/SnO₂/MWCNT nanocomposites were produced by RF plasma oxidation from the thermally evaporated pure Sn films and Sn/

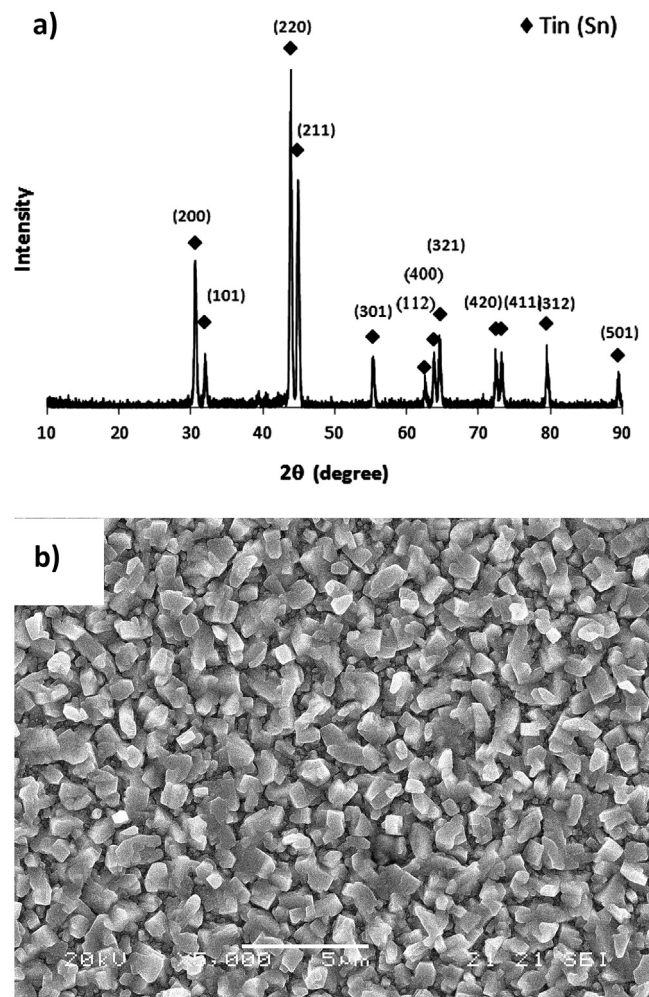


Fig. 3. a) XRD pattern and b) SEM image of pure tin (Sn) film evaporated at 1 Pa Ar pressure.

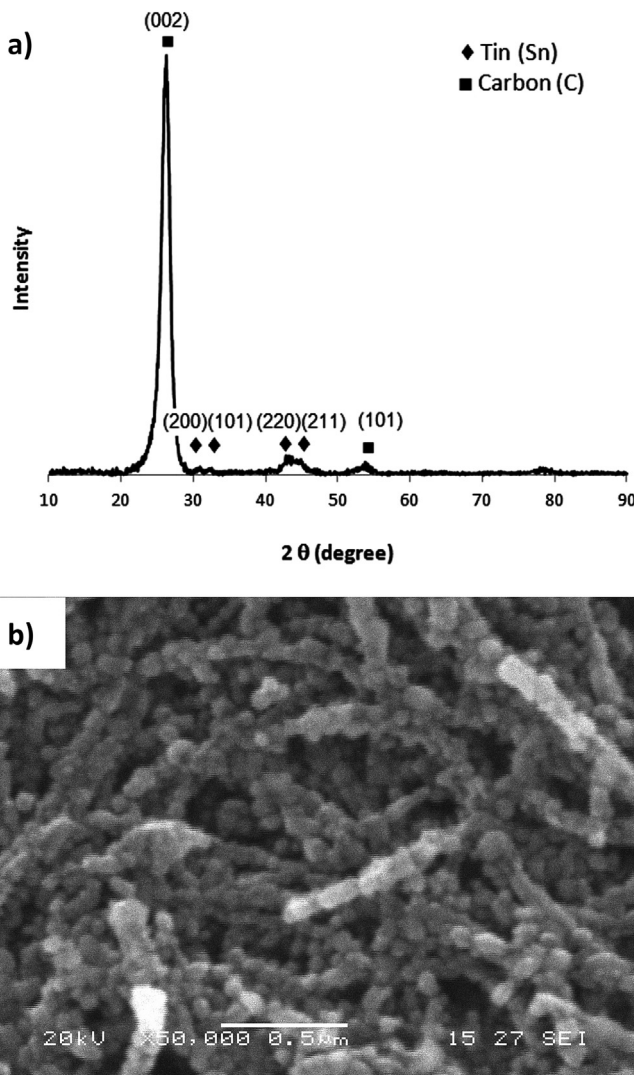


Fig. 4. a) XRD pattern of Sn/MWCNT nanocomposite and b) SEM image of Sn/MWCNT nanocomposite.

MWCNT nanocomposites, respectively. Plasma oxidation of the Sn films was conducted using high-purity oxygen (99.999%) and argon (99.9999%) gas mixture in the ratio 1:1. Three different oxidation times of 30, 45 and 60 min were chosen for obtaining different ratios of Sn:SnO₂. It was targeted to obtain a three components structure for the MWCNT reinforced nanocomposites; MWCNTs at the center, metallic Sn on the MWCNTs and plasma oxidized layer of SnO₂ on the metallic Sn layer. Total chamber pressure and RF power for each oxidation were kept constant at 1.6 Pa and 80 W, respectively. Fig. 1 schematically represents the route of preparing Sn based nanocomposite anode materials.

2.3. Characterization of nanocomposites

An X-ray diffractometer (XRD-Rigaku D/MAX 2000) with Cu-Kα radiation has been used to determine the composition, relative phase amounts and structure of the nanocomposites. Transmission electron microscopy (TEM, Tecnai G² F20 S-TWIN) and field emission gun scanning electron microscopy (FEG-SEM, JEOL 6335F) techniques were used for revealing the surface morphologies. TEM samples of the anode paper were prepared by removing a small piece of the paper and mounting it on a folding copper mesh oyster grid.

Coin-type (CR2016) test cells were assembled in an argon-filled glove box, directly using the Sn/SnO₂ coated stainless steel substrates and Sn/SnO₂/MWCNT nanocomposite free-standing electrodes as working electrodes, a lithium metal foil as the counter electrode, a micro porous polypropylene (PP) membrane (Cellgard 2300) as the separator, and 1 M solution of LiPF₆ in ethylene carbonate (EC) and dimethyl carbonate (DMC) (1:1 by weight) as the electrolyte. The cells were cyclically tested on a MTI BST8-MA Battery Analyzer at the current of 0.5 C over a voltage range of 0.1–2 V for Sn/SnO₂ on stainless steel electrodes and 0.05–3 V for Sn/SnO₂ on MWCNT buckypapers. For the rate capacity test, one selected battery was discharged at 0.25 C rate and charged at various current rates. The cyclic voltammograms were obtained over the potential range of 0.01–3 V at a scan rate of 0.2 mV s⁻¹ using Gamry Instrument Version 5.67. Electrochemical impedance spectroscopy (EIS) measurements were carried out on the samples using a sine wave of 10 mV amplitude over a frequency range of 100 kHz–0.01 Hz.

3. Results and discussion

3.1. Characteristics of buckypapers

The buckypapers were successfully produced from chemically oxidized MWCNTs as flexible, uniform, smooth and crack-free disks and easily peeled-off from PVDF membrane. Effects of oxidants on formation of MWCNT buckypaper were studied in our previous work and H₂SO₄ and HNO₃ acids in the ratio 3:1 was found most suitable for our purposes to produce MWCNT network skeleton supported electrodes [27]. FESEM surface image and cross-section of the buckypapers are shown in Fig. 2. The inset of Fig. 2a shows a photograph of the MWCNT buckypaper held by tweezers, indicating the good flexibility. Porous structure that appropriate for composite manufacturing was obtained as shown in Fig. 2b. Cross-section area of the buckypaper is homogenous and approximate thickness is 80 μm (Fig. 2c).

3.2. Characteristics of Sn films and Sn/MWCNT nanocomposites

Fig. 3 shows a typical XRD pattern for the pure tin (Sn) film evaporated onto the stainless steel substrates in an argon

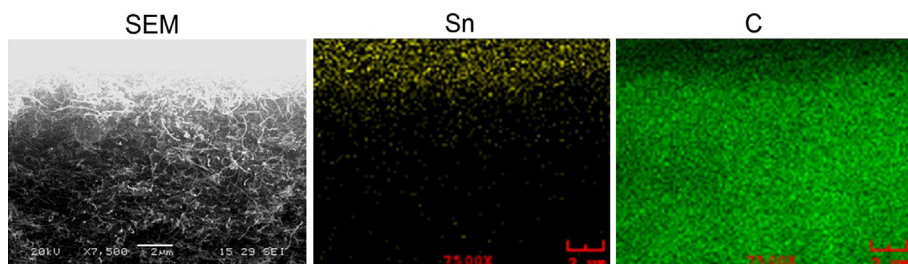


Fig. 5. SEM-EDS dot-map analysis results for Sn/MWCNT nanocomposite.

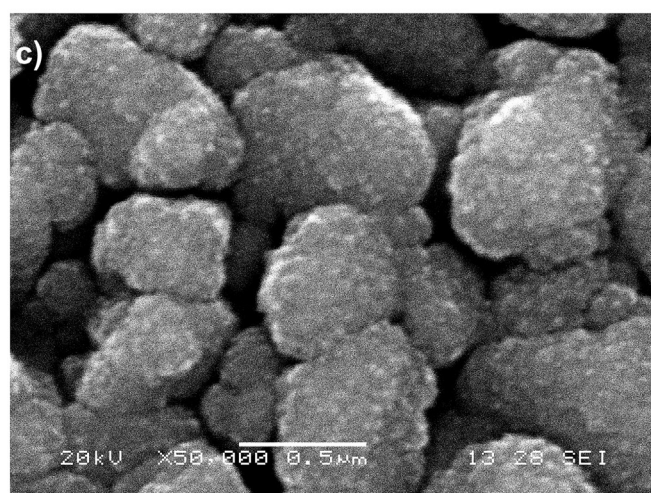
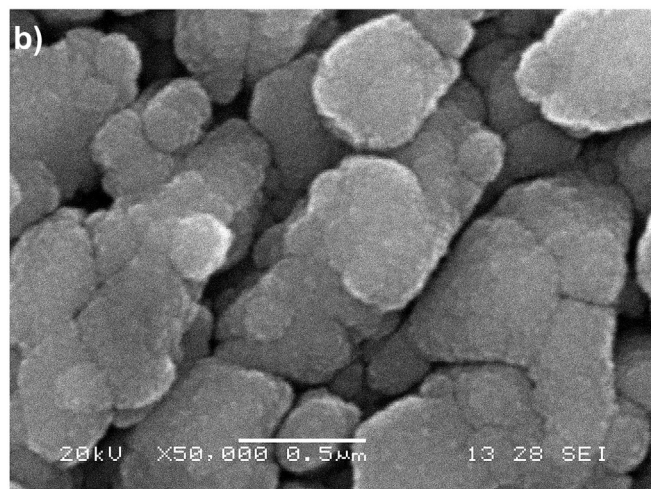
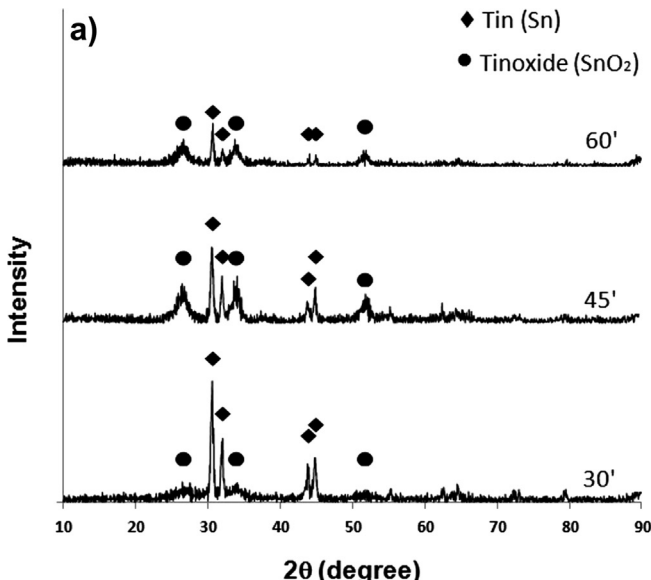
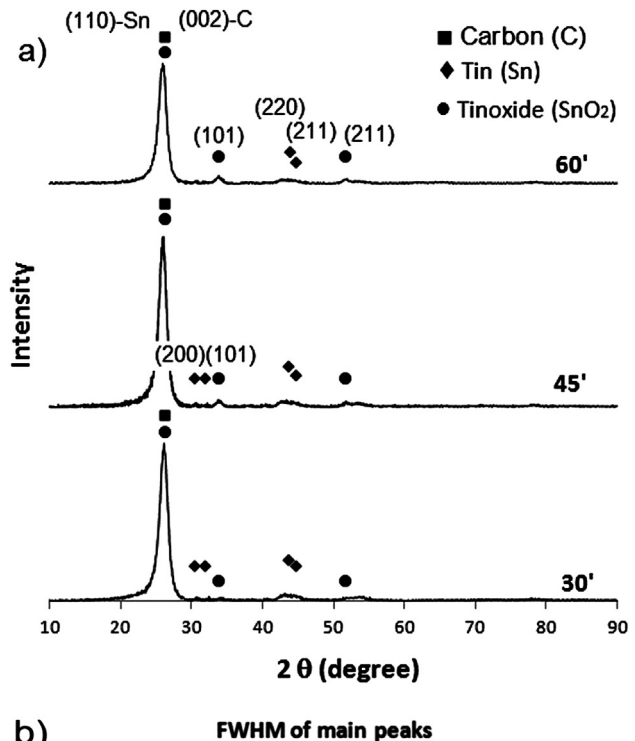


Fig. 6. a) XRD patterns of the (Sn/SnO₂) nanocomposite films b) SEM images Sn/SnO₂ nanocomposite films produced by plasma oxidation for 45 min and c) 60 min.

atmosphere at a pressure of 1.0 Pa (JCPDS file no: 01-089-2958 for powder Sn) and a SEM image. No obvious reflection peaks from impurities were detected, providing evidence of the high purity product. The (220), (211) and (200) peaks are the strongest peaks



b) FWHM of main peaks

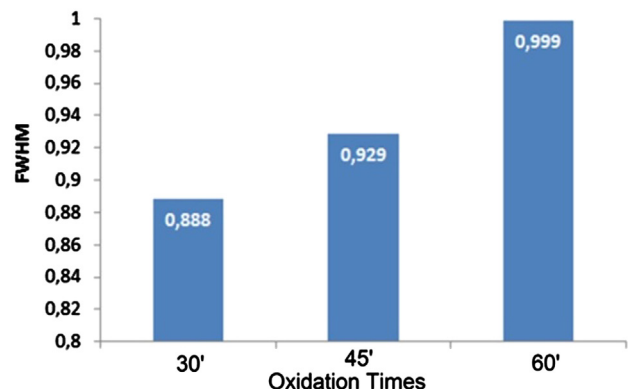


Fig. 7. a) XRD patterns of Sn/SnO₂ nanocomposite films produced by plasma oxidation for 30, 45 and 60 min and b) FWHM values of the main peaks.

observed in the film. After thermal evaporation onto a stainless steel substrate, tin exhibits a crystalline microstructure with epitaxial grains as shown in Fig. 3b. The grain size has been calculated with Scherer's formula and found 34 nm. In order to produce Sn/MWCNT nanocomposites, pure metallic tin (Sn) was thermally evaporated on the buckypapers having controlled porosity. Fig. 4a presents the XRD patterns of Sn/MWCNT nanocomposite that could be indexed as tin and carbon, with all peaks corresponding well to standard crystallographic data (Sn:JCPDS No. 01-089-2958 C:JCPDS No. 00-026-1080). No other impurities were detected, which indicates the high-purity products. SEM images of Sn/MWCNT nanocomposites are shown in Fig. 4b, which exhibits thermally evaporated Sn on the surfaces of MWCNTs forming a core–shell structure. Evaporated tin deposited not only on the surface of buckypapers but also penetrated into porous MWCNTs network. The grain size of the pure Sn on the MWCNTs has been calculated with Scherer's formula and found an average grain size of 22 nm. Fig. 4b evidences also that a homogenous porous

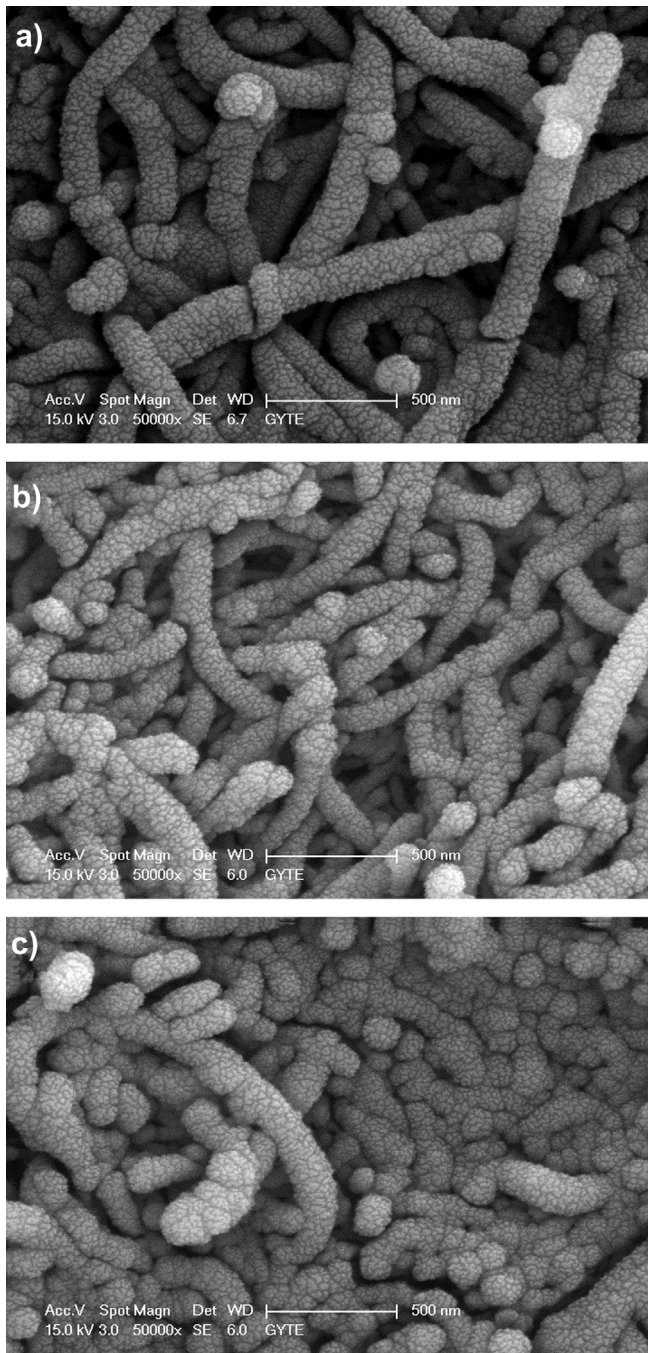


Fig. 8. FESEM images Sn/SnO₂/MWCNT nanocomposites produced by plasma oxidation for a) 30 min, b) 45 min and c) 60 min after thermal evaporation of Sn onto MWCNT buckypapers.

structure is preserved showing a 1 min thermal evaporation is proper. Microstructural investigations using SEM and TEM facilities illustrated that a maximum thickness of 40 nm Sn was deposited on the MWCNT surfaces and decreased through the center of the buckypaper producing a functionally graded composite structure. Shafiei et al. [28] produced a thin-film Sn deposited on the carbon fiber paper (CFP) composite electrode by electrodeposition and showed the SEM images similar to our surface morphology results.

Fig. 5 shows SEM-EDS dot-map analysis for Sn/MWCNT nano-composite. Sn rich layer depth is about 5 μm and evaporated tin is mainly introduced between the MWCNTs and resulted in coating on the MWCNT surfaces with remaining a significant porosity

between the MWCNTs as channels. It can be concluded from the dot-map analysis that Sn shows a gradient composition through the center of buckypaper. It is well known the gradient phase distribution in the composites is beneficial for decreasing crack initiation and therefore, failure [29]. Compositional gradient structure is a prominent characteristic in the Sn/MWCNT nanocomposite and this compositional change from the surface toward the center of the MWCNT is assessed as more beneficial for stress relaxation caused by a volume increase in the Sn/SnO₂ during Li alloying/de-alloying. It can be concluded from the dot-map analysis that Sn shows a gradient composition through the center of buckypaper. This implies that this functionally gradient structure will cause stress relaxation during the electrochemical reactions.

3.3. Characteristics of Sn/SnO₂ and Sn/SnO₂/MWCNT nanocomposites

After the thermal evaporation process, the Sn and Sn/MWCNT samples were subjected to a RF plasma oxidation process for three different oxidation times of 30, 45 and 60 min to produce Sn/SnO₂ and Sn/SnO₂/MWCNT nanocomposites. Information about the composition and the degree of crystallinity were obtained using XRD, which is presented in Fig. 6a. The films have double phases of Sn and SnO₂ structure, which agrees well with the standard data files (Sn:JCPDS No. 01-089-2958 and SnO₂:JCPDS No. 00-041-1445), and all of the films have a crystalline structure. Increasing oxidation time resulted in increasing intensity of SnO₂ peak while decreasing of Sn peak. The grain size of SnO₂ on the stainless steel substrates formed after RF plasma oxidation was calculated as 34 nm, 36 nm and 45 nm depending on RF plasma oxidation times. The phase structures of Sn/SnO₂/MWCNT composites were also analyzed by using XRD data, and the results are shown in Fig. 7. Fig. 7a shows the diffraction peaks at 26° and 33° correspond to SnO₂ (JCPDS No. 00-041-1445) while the peak at 45° for Sn (JCPDS No. 01-089-2958). Increasing oxidation time resulted in increasing intensity of SnO₂ peak. It should be noted that a diffraction peak at around 26°, which is the main peak of tetragonal SnO₂ (110) almost overlaps with the main peaks of hexagonal C (002) as also defined in the different works [30]. FWHM values of the main peaks for samples were calculated and are shown in Fig. 7b. Comparing all spectra and FWHM values, it is easy to find that broadening peaks is mainly contributing from increasing SnO₂ amount. The grain size of the SnO₂ in the Sn/SnO₂/MWCNT nanocomposites was found to be slightly dependent on the oxidation time and calculated as 26 nm, 32 nm and 36 nm by using Scherer's formula.

The SEM morphologies of Sn/SnO₂ films produced at various plasma oxidation times, including 45 and 60 min are presented in Fig. 6b, c and show very fine SnO₂ nanoparticles with increasing oxidation time. Fig. 8 presents FESEM images of Sn/SnO₂/MWCNT nanocomposites shows the effect of three different oxidation time. As seen from the images, Sn based phases were deposited around the MWCNTs forming a core–shell structure. Gao et al. [31] presented CNTs coated with thick layers of SnO₂ TEM images similar to our results. Since surface oxidation of MWCNTs creates defects on the sp² bonds, it is an expected phenomenon of nucleation and growth of Sn on the MWCNT phase. RF plasma oxidation, on the other hand, resulted in producing an outer thin layer of SnO₂ shell on the metallic pure Sn. As can be seen from the FESEM micrographs in Fig. 8, SnO₂ is formed on the surfaces with very fine nano grains, which expected to accelerate Li diffusion and, at the same time, Sn is expected to increase the conductivity together with the increased buffering effect. Indeed, we have three layers core–shell structure of MWCNTs:Sn:SnO₂. Increasing oxidation time resulted in thicker SnO₂ based phase on the MWCNT surfaces.

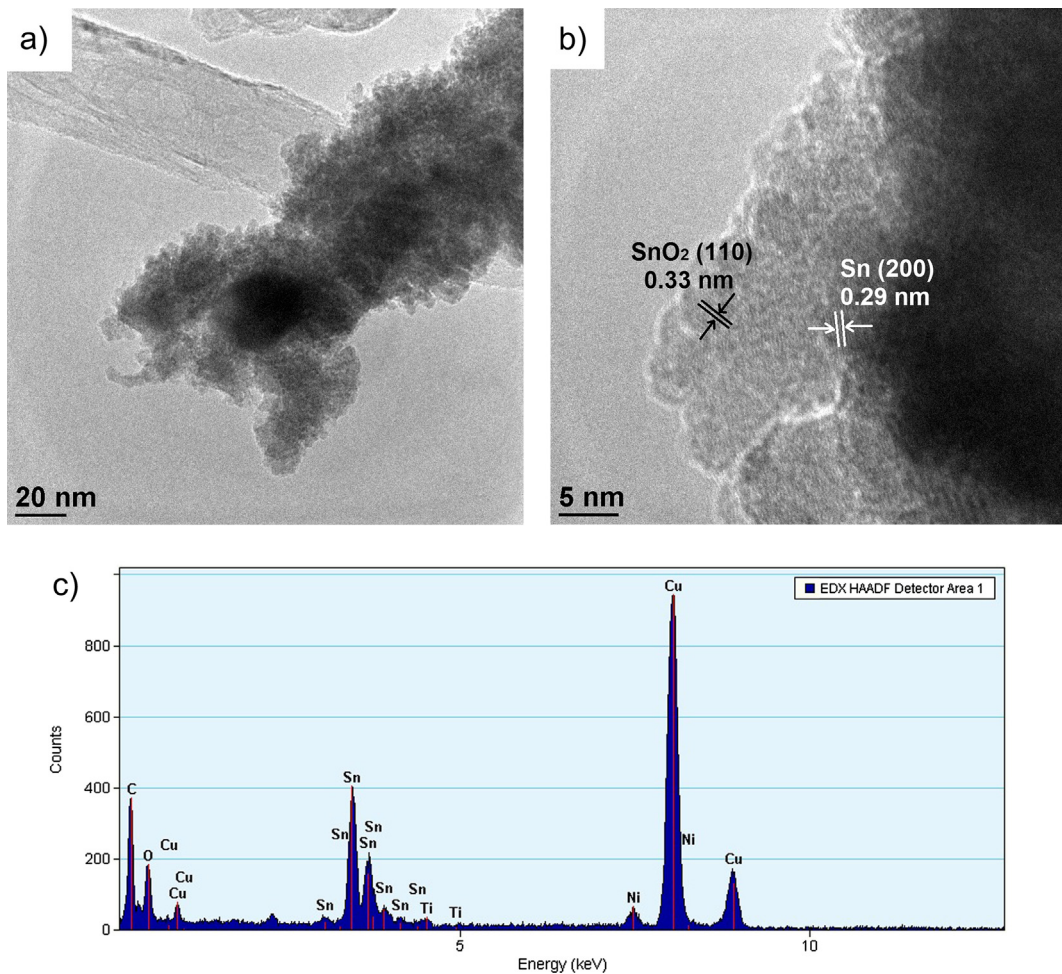


Fig. 9. TEM images (a, b) and EDS spectrum (c) of Sn/SnO₂/MWCNT nanocomposites.

Sn/SnO₂/MWCNT nanocomposites were further analyzed by transmission electron microscopy (TEM) in order to confirm the presence of Sn and SnO₂ nanoparticles onto MWCNT surfaces. TEM sample was prepared by removing a small piece of the anode paper and mounting it onto a folding copper mesh oyster grid. Fig. 9a presents image of uncoated MWCNT and coated MWCNT with Sn/SnO₂. Fig. 9b clearly implies that the crystal size of the deposited Sn/SnO₂ is very fine and shows the lattice fringes of Sn and SnO₂ nanoparticles. As can be seen from Fig. 9c, carbon, tin and oxygen peaks are clearly visible and copper and nickel peaks, which come from the sample holder.

Quantitative phase analysis of all nanocomposites was performed in order to determine the relative phase amounts using Rietveld refinement method with helping Rigaku Software, as shown in Table 1. Increasing oxidation time resulted in increasing

SnO₂ percent and decreasing Sn. If the MWCNTs are assumed to be omitted, the calculations showed that the amount of Sn that oxidized to SnO₂ on the MWCNT surfaces from the pure Sn was higher compared with Sn coated on stainless steel substrates. This is attributed to the higher surface area of the Sn coating and obtaining finer Sn depositions on the MWCNTs by thermal evaporation since the nucleation effect of the carbon nanotubes.

3.4. Electrochemical results

Cyclic voltammetry (CV) measurements were performed to examine the electrochemical properties of electrodes during the charge–discharge process for the first three cycles. Results of cyclic voltammetry of Sn/SnO₂ nanocomposite thin films and Sn/SnO₂/MWCNT nanocomposite electrodes for the first three cycles depending on the plasma oxidation time were shown in Fig. 10. In Fig. 10a–c, the small cathodic peak around 1.34 V and the peak at 0.34 V are due to the reduction of SnO₂ to elemental Sn (Eq. (1)) and the solid electrolyte interface (SEI) formation during the first discharge. SEI formation is caused by the decomposition of the electrolyte and the lithium salt at the surface of the electrode, and both peaks disappear after the first cycle. Since the production of Li₂O and SEI formation are known as the irreversible reaction, the reaction corresponding to the alloying of lithium with Sn is only considered reversible for the subsequent lithium insertion cycle as also reported by Dongjoon Ahn et al. [32];

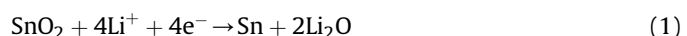


Table 1

Percent of phase ratio of Sn/SnO₂ and Sn/SnO₂/MWCNT nanocomposites.

Electrodes	% C	% Sn	% SnO ₂
Sn/SnO ₂ 30 min	—	82	18
Sn/SnO ₂ 45 min	—	74	26
Sn/SnO ₂ 60 min	—	64	36
Sn/SnO ₂ /MWCNT 30 min	73	5	22
Sn/SnO ₂ /MWCNT 45 min	68	15	17
Sn/SnO ₂ /MWCNT 60 min	63	28	8

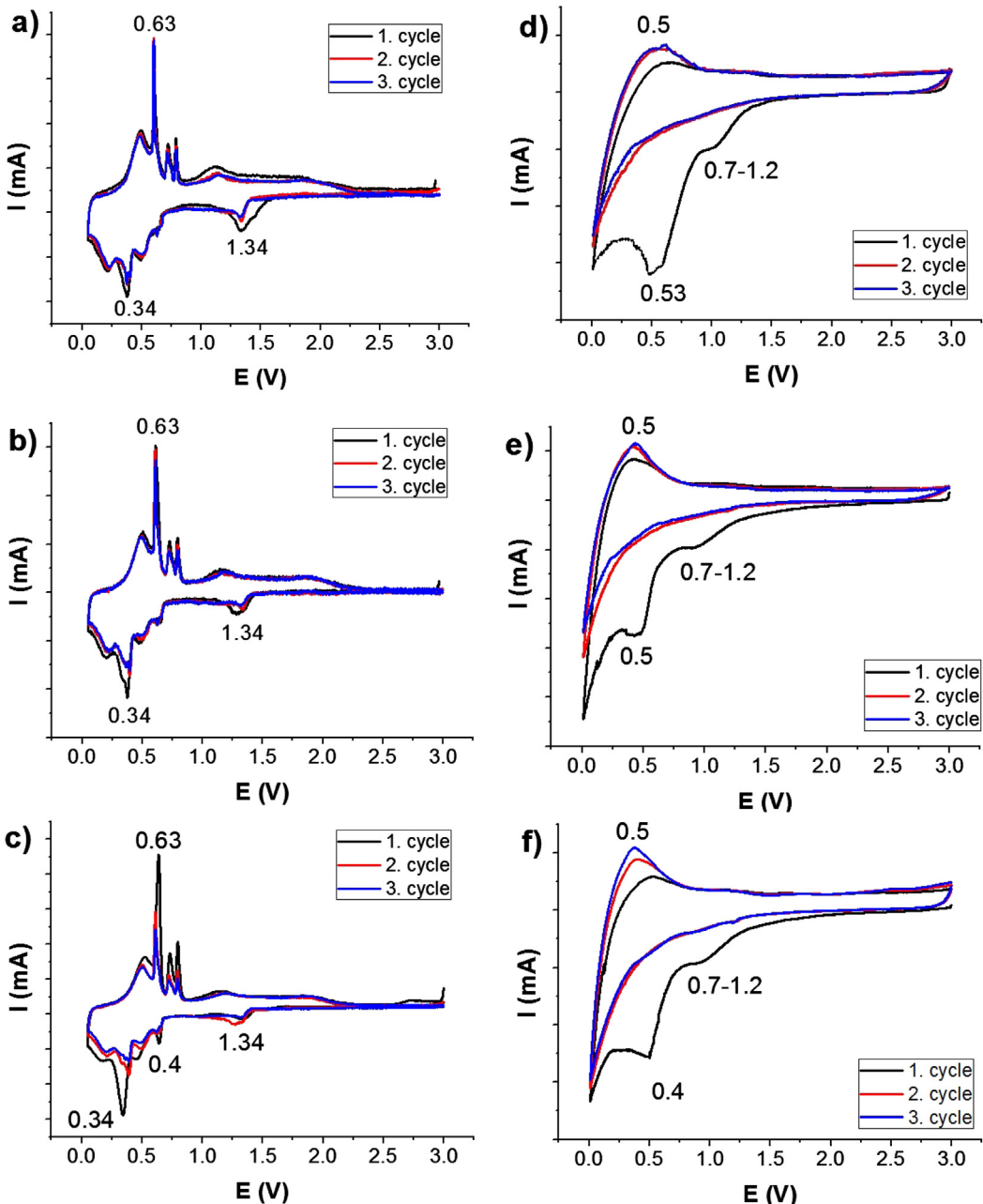


Fig. 10. Cyclic voltammograms for the first 3 cycles of the electrodes at a scan rate of 0.2 mV s^{-1} . (a) Sn/SnO₂-30 (b) Sn/SnO₂-45 (c) Sn/SnO₂-60 (d) Sn/SnO₂/MWCNT-30 (e) Sn/SnO₂/MWCNT-45 (f) Sn/SnO₂/MWCNT-60.

Depending on oxidation time and hence the phase ratios of SnO₂ in Sn/SnO₂ nanocomposites, the first discharge peaks showed various intensities. Increasing percentage ratio of SnO₂, caused to reduce the capacity fades in the first cycle because of the contribution the capacity by the reduction of SnO₂ to element Sn [6]. The cathodic peaks below 0.4 V are due to formation of the Li_xSn alloy. The noise in these peaks is due to the multi-stage lithium intercalation of Li_xSn alloys [33]. The anodic peak at 0.63 V corresponds to the de-alloying reaction of Li_xSn (Eq. (2)). These two reactions are fully reversible.

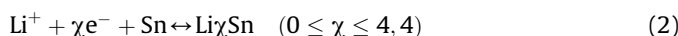


Fig. 10d–f shows CV curves for Sn/SnO₂/MWCNT free standing nanocomposite electrodes that evaporated for 1 min and plasma

oxidized for 30 min, 45 min and 60 min at Ar:O₂ (1:1) gas mixture. There is a strong peak at about 0.53 V during the first discharge process, due to the formation of the solid electrolyte interphase (SEI) layer. This strong peak observed in the Sn/SnO₂/MWCNT electrodes, as shown in Fig. 8d–f 0.53 V was also reported by Zhang et al. [34] in the SnO₂/CNT core–shell structures during the first cathodic sweep, which tended to disappear in the following cycles. This feature was ascribed to the electrolyte decomposition on the surface of the CNTs and a resulting solid electrolyte interface (SEI) film formation. The reduction peak in the range of 0.7–1.2 V corresponds to decomposition of SnO₂ to become Sn as in Eq. (1) which only happens in the first discharge cycle. An oxidation peak at 0.5 V corresponds to the reversible formation of Li_xSn alloys (Eq. (2)).

The discharge capacity vs. the number of cycles for cells made from Sn/SnO₂ films is shown in Fig. 11a. The results show that the

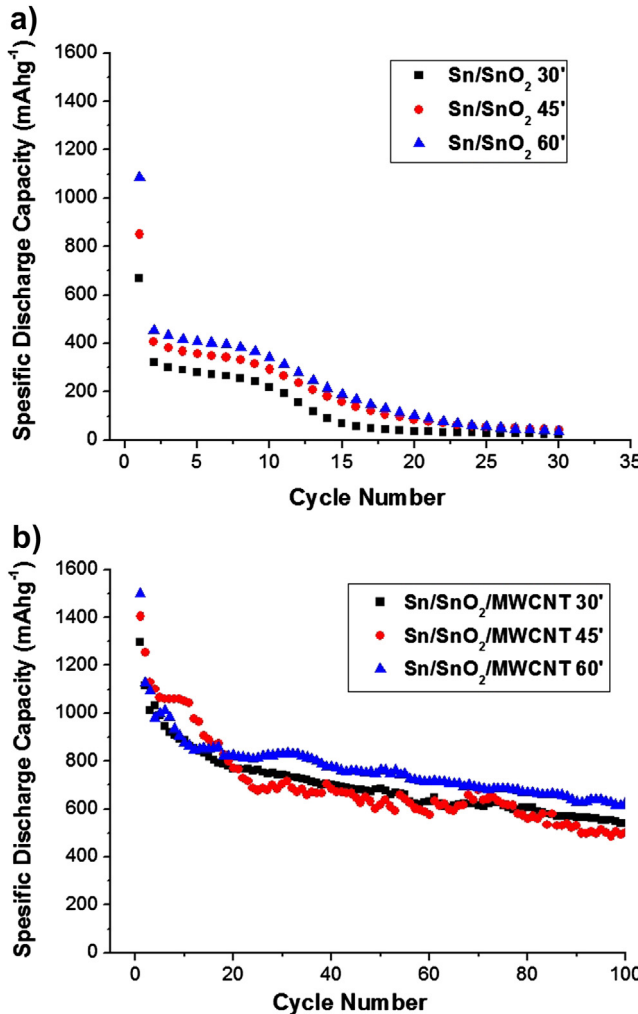


Fig. 11. Specific discharge capacities of (a) Sn/SnO₂ nanocomposite films electrodes and (b) Sn/SnO₂/MWCNT free-standing electrodes depending on plasma oxidation times.

specific discharge capacities of the Sn/SnO₂ films increases with increasing amount of SnO₂ in the nanocomposites. Similar relationship between SnO₂ ratio and specific capacity values have been obtained by Sivashanmugam et al. [6]. Although, relatively high discharge capacities were obtained in the Sn/SnO₂ double phase electrodes, very low capacity retention is seen to be the obstacle for these electrodes. The cells assembled from Sn/SnO₂ on the stainless steel were failed after approximate 25–30 cycles. It is believed because of Sn based electrode disintegration caused by a high-volume increase [18].

Compared with the Sn/SnO₂ double phase structures on the stainless steel coin electrodes, the Sn/SnO₂/MWCNT nanocomposites showed outstanding performance with high capacity and satisfactory cycling stability. Even at 100 cycles no cell failure was detected in all the studied cell assemblies. Fig. 11b displays cycling stability of the Sn/SnO₂/MWCNT nanocomposite electrodes at the voltage range between 0.5 and 3 V. The capacity retention for the first 10 cycles is maintained as 68%, 78% and 58% for the Sn/SnO₂/MWCNT nanocomposites electrodes plasma oxidized for 30, 45 and 60 min, respectively. At 100 cycles, the discharge capacities are still 540, 500, 624 mAh g⁻¹ and capacity retentions after 50 cycles are 41%, 35% and 41% for the Sn/SnO₂/MWCNT nanocomposites electrodes, oxidized for 30, 45 and 60 min, respectively.

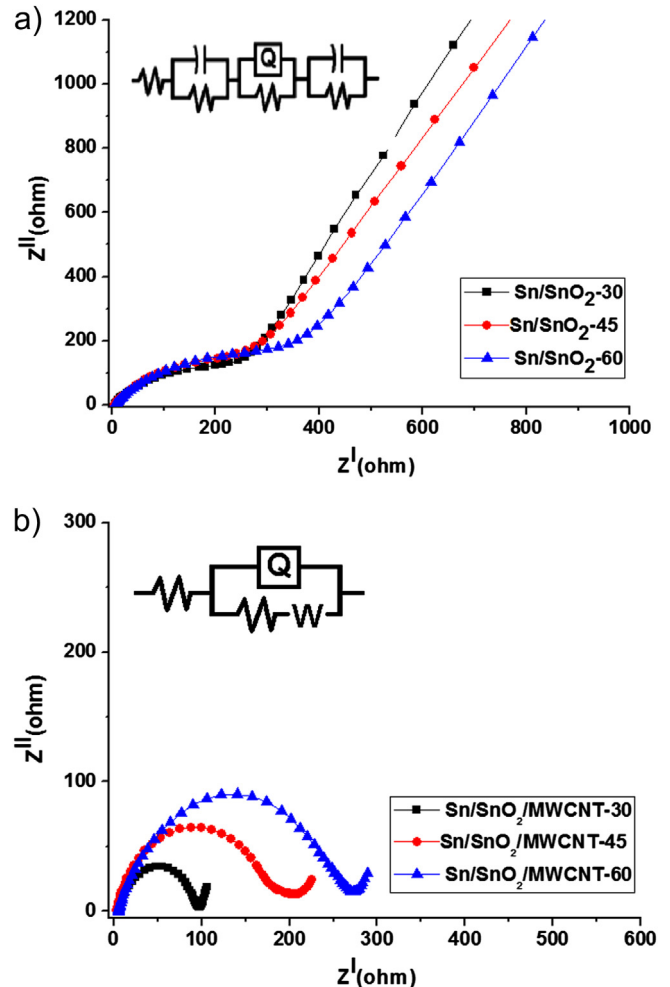


Fig. 12. Electrochemical impedance spectra of (a) Sn/SnO₂ and (b) Sn/SnO₂/MWCNT nanocomposite electrodes.

Electrochemical Impedance Spectroscopy (EIS) measurements were carried out to confirm the effect of MWCNTs and plasma oxidation time on changing the charge transfer resistance in Sn/SnO₂ and Sn/SnO₂/MWCNT nanocomposite electrodes using a sine wave of 10 mV amplitude over a frequency range of 100 kHz–0.1 Hz. Fig. 12 shows the Nyquist plots obtained from the Li-ion cells before testing electrochemical performance. The intercept at the Z_{real} axis at high frequency corresponds to the ohmic resistance (R_{Ω}), which represents the total resistance of the electrolyte, separator, and electrical contacts. The depressed semicircle in the middle frequency range relates to the charge transfer resistance (R_{ct}). The inclined line at lower frequency represents the Warburg impedance (W), which is associated with Li-ion diffusion in the SnO₂ particles. An equivalent circuit model was constructed to

Table 2
Impedance parameters of calculated from equivalent circuit model.

Electrodes	Circuit model	R_s (Ω)	R_{ct} (Ω)
Sn/SnO ₂ -30'	[R(CR)(QR)(CR)]	5.2	287
Sn/SnO ₂ -45'		5.2	302
Sn/SnO ₂ -60'		5.5	437
Sn/SnO ₂ /MWCNT-30'	[R(Q(RW))]	7.13	379
Sn/SnO ₂ /MWCNT-45'		7.46	358
Sn/SnO ₂ /MWCNT-60'		7.51	257

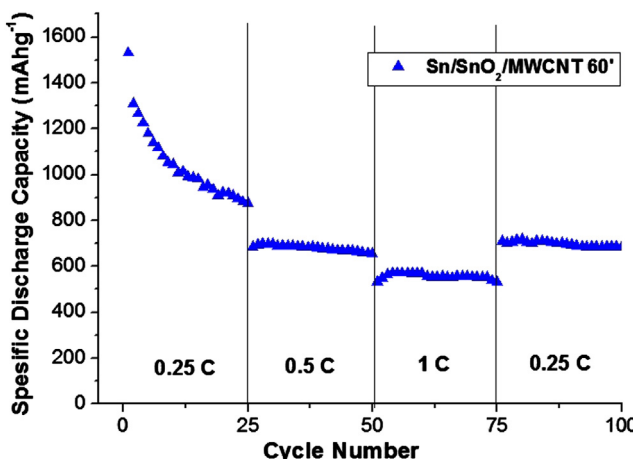


Fig. 13. Rate capacity of Sn/SnO₂/MWCNT nanocomposite oxidized for 60 min. The voltage window is 0.1–2 V.

analyze the impedance spectra, as shown in the inset to Fig. 12. Table 2 shows parameters of the equivalent circuit for the Sn/SnO₂ and Sn/SnO₂/MWCNT nanocomposite electrodes after fitting the diameter of the semicircular curve.

The a.c. impedance measurements confirm that both interface resistance and charge-transfer resistance for the Sn/SnO₂ and Sn/SnO₂/MWCNT nanocomposite electrodes gradually decrease with the increasing oxidation time. Therefore, it is reasonable to believe that good electrode electron contact and electrical conductivity are important for excellent electrochemical performance. Another reason for increased electrochemical performance in the Sn/SnO₂/MWCNT nanocomposites is the compact and stout wall of the MWCNTs accommodates large volume expansion, cushioning against the large internal stresses caused by tin aggregation during charge/discharge cycles and allowing excellent cycle duration by preventing electrode pulverization [10,22,35]. The data shown in Fig. 12 also proves that the MWCNT contained nanocomposite obtained with 60 min oxidation time yielded lowest charge transfer resistance, which we have attributed to the highest SnO₂ content with a decreased amount of Sn aggregates and unique functionally gradient nature obtained in this study with the two steps production method. Table 2 shows impedance parameters obtained from the Li-ion cells before testing electrochemical performance.

Fig. 13 displays the rate performance of the electrode made from Sn/SnO₂/MWCNT nanocomposite oxidized for 60 min at various C-rates ranging from 0.25 to 1 C. As the current density increased from 0.5 to 1 C, the discharge capacity decreased slightly from 710 to 661 mAh g⁻¹. When the current density was decreased from 1 C to 0.25 C the discharge capacity produced the same capacity of approximately to 710 mAh g⁻¹, revealing the superior reversibility of the Sn/SnO₂/MWCNT gradient nanocomposite and their suitability as a high rate anode material.

4. Conclusions

Double phase Sn/SnO₂ nanocomposite films and Sn/SnO₂/MWCNT core–shell nanocomposites were produced by a two steps processes, first thermal evaporation, and subsequent plasma oxidation as anode materials for Li-ion batteries. Plasma oxidation time was changed to investigate of the effects of Sn:SnO₂ ratio on the stainless steel substrate and MWCNT buckypapers. It was proven that the electrodes have double phase, core–shell and nanostructure properties by using SEM, TEM and XRD facilities. Li-ion cells were built up using Sn/SnO₂ nanocomposite film

electrodes and free-standing Sn/SnO₂/MWCNT electrodes. Cyclic voltammetry (CV) measurements showed electrochemical reactions according to Sn:SnO₂ ratio in nanocomposite electrodes. The Sn/SnO₂/MWCNTs showed a reversible discharge capacity of 1500 mAh g⁻¹ in the first cycle because of the advantageous geometrical features of the highly conductive nanocomposite network and the optimized ratio of Sn/SnO₂ with a gradient composition of Sn highest at the surface a gradual decrease through the center of MWCNT buckypaper with a core–shell structure. Sn/SnO₂ electrodes produced on the stainless steel failed almost in 25–30 cycles. Sn/SnO₂/MWCNT electrodes maintained a high capacity (624 mAh g⁻¹ for Sn/SnO₂/MWCNT oxidized for 60 min) even after 100 cycles because of various beneficial factors, such as size-dependent effects, facial electron transport, minimization of aggregation of the nanoparticle, providing gradient composition of active phases, and alleviation of huge volume expansion, originating from the merits of each material and the advantageous geometrical features. Rate capability of the same electrode produced excellent capacity recovery between 0.25 and 1 C. We anticipate that this approach using a controllable gradient composition, oxidation of Sn process will open up new opportunities for the use of other Li-alloying metals as well as various transition-metal oxides in the development of high-performance Li-ion batteries with high Li storage and long-term cycling lives.

Acknowledgments

This work is supported by the Scientific and Technological Research Council of Turkey (TUBITAK) under the contract number 109M464 – Improving the Capacity of Li-Ion Batteries by Using New Semi-Conducting Metal Oxide Based Anodes. The authors thank the TUBITAK MAG workers for their financial support and Sakarya University, Coordination of Scientific Research Project (BAPK) under the contract number 2010-50-02-017.

References

- [1] E.M. Krieger, C.B. Arnold, *J. Power Sources* 210 (2012) 286–291.
- [2] C. Casas, W. Li, *J. Power Sources* 208 (2012) 74–85.
- [3] J. Chen, *Materials* 6 (2013) 156–183.
- [4] G.R. Goward, N.J. Taylor, D.C.S. Souza, L.F. Nazar, *J. Alloys Compd.* 329 (2001) 82–91.
- [5] C. Lupu, J.-G. Mao, J.W. Rabalais, A.M. Guloy, J.W. Richardson, *Inorg. Chem.* 42 (2003) 3765–3771.
- [6] A. Sivashanmugam, T.P. Kumar, N.G. Renganathan, S. Gopukumar, M. Wohlfahrt-Mehrens, J. Garche, *J. Power Sources* 144 (2005) 197–203.
- [7] G. Liu, X. Shen, K. Uo, L. Wang, N. Kumagai, *J. Power Sources* 217 (2012) 108–113.
- [8] T. Zhang, L.J. Fu, J. Gao, Y.P. Wu, R. Holze, H.Q. Wu, *J. Power Sources* 174 (2007) 770–773.
- [9] M. Wu, C. Wang, J. Chen, F. Wang, B. Yi, *Ionics* (2013), <http://dx.doi.org/10.1007/s11581-013-0870-9>.
- [10] M. He, L. Yuan, X. Hu, W. Zhang, J. Shu, Y. Huang, *Nanoscale* 5 (2013) 3298–3305.
- [11] M. Gu, Y. Li, X. Li, S. Hu, X. Zhang, W. Xu, S. Thevuthasan, D.R. Baer, J.G. Zhang, J. Liu, C. Wang, *ACS Nano* 6 (2012) 8439–8447.
- [12] C.M. Wang, W. Xu, J. Liu, J.G. Zhang, L.V. Saraf, B.W. Arey, D. Choi, Z.G. Yang, J. Xiao, S. Thevuthasan, *Nano Lett.* 11 (2011) 1874.
- [13] C. Wang, Y. Zhou, M.Y. Ge, X.B. Xu, Z.L. Zhang, J.Z. Jiang, *J. Am. Chem. Soc.* 132 (2010) 46.
- [14] H. Zhao, G. Zhang, C. Jiang, X. He, *Ionics* 18 (2012) 11–18.
- [15] C. Bonino, L.W. Ji, Z. Lin, O. Toprakci, X.W. Zhang, S.A. Khan, *ACS Appl. Mater. Interfaces* 3 (2011) 2534.
- [16] J. Kong, Z. Liu, Z. Yang, H.R. Tan, S. Xiong, S.Y. Wong, X. Li, X. Lu, *Nanoscale* 4 (2012) 525.
- [17] Y. Kim, Y. Yoon, D. Shin, J. Anal. Appl. Pyrol. 85 (2009) 557–560.
- [18] Y. Fu, M. Ma, Y. Shu, Z. Cao, X. Ma, *Mater. Lett.* 63 (2009) 1946–1948.
- [19] J. Ren, J. Yang, A. Abouimrane, D. Wang, K. Amine, *J. Power Sources* 196 (2011) 8701–8705.
- [20] H. Buqa, M. Holzapfel, F. Krumeich, C. Veit, P. Novak, *J. Power Sources* 161 (2006) 617–622.
- [21] K. Aifantis, S. Hackney, J. Dempsey, *J. Power Sources* 165 (2007) 874–879.

- [22] Y. Zhao, J. Li, N. Wang, C. Wu, G. Dong, L. Guan, *J. Phys. Chem. C* 116 (2012) 18612–18617.
- [23] Y.H. Jin, K.M. Min, S.D. Seo, H.W. Shim, D.W. Kim, *J. Phys. Chem. C* 115 (2011) 22062.
- [24] Y. Chen, Q. Huang, J. Wang, Q. Wang, J. Xue, *J. Mater. Chem.* 21 (2011) 17448.
- [25] X. Wang, X. Cao, L. Bourgeois, H. Guan, S. Chen, Y. Zhong, D.M. Tang, H. Li, T. Zhai, L. Li, Y. Bando, D. Golberg, *Adv. Funct. Mater.* 22 (2012) 2682.
- [26] G.Jeong, C.Shin, Y.-J.Kim, H.Lee, H.-J.Sohn, *Electrochim. Acta* 92 (2013) 291–297.
- [27] U. Tocoglu, M. Alaf, O. Cevher, M.O. Guler, H. Akbulut, *J. Nanosci. Nanotechnol.* 12 (2012) 9169–9174.
- [28] M. Shafiei, A.T. Alpas, *J. Power Sources* 196 (2011) 7771–7778.
- [29] M.T. Tilbrook, R.J. Moon, M. Hoffman, *Compos. Sci. Technol.* 65 (2005) 201–220.
- [30] W. Han, A. Zettl, *Nano Lett.* 3 (2003) 681–683.
- [31] L. Zhao, L. Gao, *Carbon* 42 (2004) 1858–1861.
- [32] D. Ahn, X. Xiao, Y. Li, A.K. Sachdev, H.W. Park, A. Yu, Z. Chen, *J. Power Sources* 212 (2012) 66–72.
- [33] C.H. Yim, E.A. Baranova, F.M. Courtel, Y. Abu-Lebdeh, I.J. Davidson, *J. Power Sources* 196 (2011) 9731–9736.
- [34] H. Zhang, H. Song, X. Chen, J. Zhou, H. Zhang, *Electrochim. Acta* 59 (2012) 160–167.
- [35] M. He, L. Yuan, X. Hu, W. Zhang, J. Shu, Y. Huang, *Nanoscale* 5 (2013) 3298.